scientific reports

Longitudinal investigation of changes in resting-state co-activation patterns and their predictive ability in the zQ175 DN mouse model of Huntington's disease

Mohit H. Adhikari[1,2,5]✉, Tamara Vasilkovska[1,2,5], Roger Cachope[3], Haiying Tang[3], Longbin Liu[3], Georgios A. Keliris[4], Ignacio Munoz-Sanjuan[3], Dorian Pustina[3], Annemie Van der Linden[1,2] & Marleen Verhoye[1,2]

Huntington's disease (HD) is a neurodegenerative disorder caused by expanded (≥ 40) glutamine-encoding CAG repeats in the huntingtin gene, which leads to dysfunction and death of predominantly striatal and cortical neurons. While the genetic profile and clinical signs and symptoms of the disease are better known, changes in the functional architecture of the brain, especially before the clinical expression becomes apparent, are not fully and consistently characterized. In this study, we sought to uncover functional changes in the brain in the heterozygous (HET) zQ175 delta-neo (DN) mouse model at 3, 6, and 10 months of age, using resting-state functional magnetic resonance imaging (RS-fMRI). This mouse model shows molecular, cellular and circuitry alterations that worsen through age. Motor function disturbances are manifested in this model at 6 and 10 months of age. Specifically, we investigated, longitudinally, changes in co-activation patterns (CAPs) that are the transient states of brain activity constituting the resting-state networks (RSNs). Most robust changes in the temporal properties of CAPs occurred at the 10-months time point; the durations of two anti-correlated CAPs, characterized by simultaneous co-activation of default-mode like network (DMLN) and co-deactivation of lateral-cortical network (LCN) and vice-versa, were reduced in the zQ175 DN HET animals compared to the wild-type mice. Changes in the spatial properties, measured in terms of activation levels of different brain regions, during CAPs were found at all three ages and became progressively more pronounced at 6-, and 10 months of age. We then assessed the cross-validated predictive power of CAP metrics to distinguish HET animals from controls. Spatial properties of CAPs performed significantly better than the chance level at all three ages with 80% classification accuracy at 6 and 10 months of age.

Huntington's disease is an autosomal dominant, neurodegenerative disorder that manifests itself typically in adulthood as a combination of motor and cognitive symptoms that worsen progressively[1]. Neuropsychiatric symptoms such as depressed mood, mania, anxiety, obsessions-compulsions, and psychosis have also been reported in HD patients[2]. HD is caused by expanded (≥ 40) glutamine-encoding CAG repeats in the huntingtin gene that lead to the expression of mutant huntingtin (mHTT)[3]. Brain regional atrophy starts in the striatum and as the disease progresses the degeneration expands to cortical regions[4,5]. As in case of other neurodegenerative diseases such as Alzheimer's disease (AD) and Parkinson's disease, neurodegeneration in HD can start before the appearance of clear behavioral signs. Neuroimaging investigations can contribute greatly in identifying disease

[1]Bio-Imaging Lab, University of Antwerp, Antwerp, Belgium. [2]μNEURO Research Centre of Excellence, University of Antwerp, Antwerp, Belgium. [3]CHDI Management for CHDI Foundation, Princeton, NJ, USA. [4]Institute of Computer Science, Foundation for Research and Technology - Hellas, Heraklion, Crete, Greece. [5]These authors contributed equally: Mohit H. Adhikari and Tamara Vasilkovska. ✉email: mohit.adhikari@uantwerpen.be

markers before making a clinical motor diagnosis. Resting-state functional magnetic resonance imaging (RS-fMRI), in particular, has been a promising tool in developing such biomarkers for a number of neurological as well as neurodegenerative disorders such as stroke[6,7], disorders of consciousness[8] and AD[9]. In AD, alterations in the functional connectivity (FC) of the default mode network (DMN), the most prominent of the resting-state networks (RSNs), have been shown to correlate with amyloid-β deposits[10]. In the case of HD, alterations in the RS-FC have been found in several RSNs including visual, somato-motor, executive, auditory and cerebellar networks[11–13], mostly during the manifest stage of the disease. However, the findings have not been consistent in regards to the directionality of the change in patients vis-à-vis healthy participants[14].

Most investigations of RS-FC in HD have relied on the methods of static analysis of RS-fMRI data, namely the seed-based analysis, independent component analysis or graph-theoretical analysis on the static FC[14]. The assumption underlying these analysis methods is that an estimate of FC derived from the entire duration of a RS scan is a robust representation of the subject's brain state. This assumption, however, ignores temporal fluctuations of FC over the duration of the scan that reveal the brain dynamics at shorter timescales constituting the FC and RSNs. In the last decade, novel techniques to extract dynamic changes in the RS data during a scan have been developed[15–17]. One stream in this emerging research domain has focused on quantifying variations within the static FC and testing the non-stationarity of FC with rigorous methods[18,19]. Another stream investigates the topology and dynamics of transient brain-states that constitute the RSNs and their neural correlates[20–23]. Co-activation patterns (CAPs)[20] are an example of patterns of brain activity that can be extracted from the dynamical analysis of RS-fMRI data representing blood-oxygenation-dependent (BOLD)-based transient brain states that are obtained at a single time frame resolution (i.e., at every measured fMRI volume). Another example is the quasi-periodic patterns, which are recurring spatiotemporal patterns of BOLD activity of fixed temporal length[22,24]. The time-varying information extracted with these methods has shown that traditional static FC analyses conceal important clues on the temporal dynamics of brain activity, such as the specific micro-states, their occurrence, their order, and their duration. Such information can provide additional features with promising value for being a sensitive biomarker in neurodegenerative diseases like HD.

Here we investigated, longitudinally, changes in the RS-CAPs that are transient constituents of RSNs in a mouse model of HD. The mouse model is the knock-in heterozygous (HET) zQ175 delta-neo (DN) that shows molecular, cellular and circuitry alterations that resemble those observed in people with HD (PwHD)[25–27]. In this mouse model, motor disturbances are manifested at 6-months of age and worsen at 10 months of age[25]. We acquired longitudinal RS-fMRI data in wild-type (WT) and HET animals at 3, 6, and 10 months of age. We identified CAPs using a recently developed method[28] at each age. We hypothesized that the impact of mutant huntingtin (mHTT) will be reflected in the spatial (activation pattern) and temporal (frequency and duration) components of prominent and physiologically informative RS-CAPs at all ages including the 3-months time point. We further hypothesized that reliable CAP metrics should be able to accurately predict the identity of HET mice and paid particular attention to their ability to classify animals at the earliest time point of 3 months of age.

Results

CAP identification.

We started by identifying the optimal number of CAPs at each age. Figure 1 shows the total variance explained across subjects by each partition of the concatenated image-series from all subjects (18 WT and 19 HET). Visual identification of the elbow point of this curve that also ensured less than 0.5% gain in variance beyond it (bottom panels, Fig. 1) showed partitions with 8, 3, and 6 clusters at the 3, 6, and 10-months time points, respectively, were optimal. As the three time points showed there was a quite differently explained variance versus number of clusters curves (in particular, the 6-months time point from the other two), we decided to perform the CAP analysis separately at each time point. CAPs were obtained by averaging the z-scored BOLD signals, voxel-wise, across all time frames with identical cluster membership.

Description of CAPs: temporal and spatial features.

Figure 2 shows the first four of the 8 CAPs found at the 3 months time point. The genotype group-wise spatial pattern for each CAP (top panels, A, D, G, J) is represented by the color-coded t-value of voxels that show significant non-zero activation or deactivation ($p < 0.01$, one-sample T-test, Bonferroni corrected for the number of voxels) within the WT or the HET group. The bottom panels of Fig. 2A, D, G and J show the t-statistic values for voxels that show a significant inter-genotype difference (WT-HET) in activation ($p < 0.05$, 2-sample T-test, FDR corrected). The first CAP (LCN CAP; Fig. 2A) is characterized by simultaneous co-deactivations of the mouse default-mode-like network (DMLN) composed of anterior cingulate, orbital, visual, retrosplenial, entorhinal cortices as well as dorsal hippocampus, and co-activations of lateral-cortical network (LCN) constituted by somatosensory, motor, and frontal association cortices as well as the caudate putamen. The spatial patterns of the second CAP (DMLN CAP, Fig. 2D) showed a pattern anti-correlated with the LCN CAP. The remaining six CAPs could also be grouped in three spatially anti-correlated pattern pairs (Figs. 2G, J, Supplementary Fig. 1A, D, G, J). CAPs 3 and 4 (Figs. 2G and J) show widespread cortico-striatal co-deactivation and co-activation, respectively. Importantly, spatial topology of the first four CAPs is qualitatively very similar to those found by Gutierrez-Barragan et al.[28], 2019. Figure 2C, E, F, H, I and K, L show the comparison of the distribution of subject-wise temporal properties—duration and occurrence percentage—of each CAP between the WT and HET group. Supplementary Fig. 1 shows the spatial patterns and inter-group comparisons of spatial and temporal properties of four remaining CAPs identified at the 3 months time point. None of the CAPs showed any significant inter-genotype difference in either the duration or the occurrence percentage.

Figure 3 shows the spatial patterns in the WT & HET group as well as inter-group comparison of spatial and temporal properties of the three CAPs identified at the 6-months time point. As in the case of the 3 months time point, the first two CAPs were characterized by simultaneous co-deactivation of DMLN and co-activation of LCN

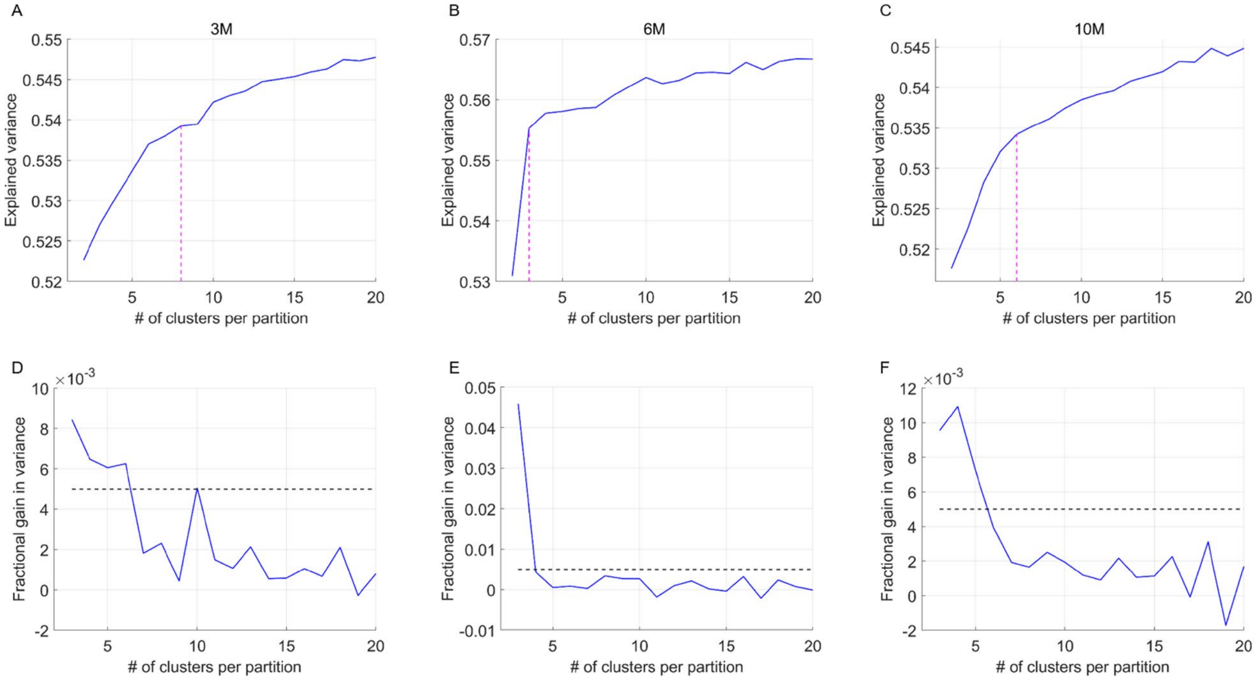

Figure 1. (**A**)–(**C**) Across-subject variance explained as a function of number of clusters in the partition of the combined image-series at the 3 months (**A**), 6-months (**B**) and the 10-months (**C**) time points. Magenta dashed line indicates the elbow point beyond which the explained variance is found to saturate in each case. We found 8, 3 and 6 clusters were sufficient to explain ~ 53–55% of variance at the 3, 6 and 10-months time points respectively. (**D**)–(**F**) Fractional gain in the explained variance as the number of clusters in the partition increase from k to k + 1, as a function of partitions, for 3 months (**D**), 6-months (**E**) and the 10-months (**F**) time points. We find that the fractional gain for every k after the elbow point is lower that 0.5%.

and vice versa, respectively. CAP 3 showed the widespread co-deactivation of cortical-striatal regions. None of the three CAPs showed any significant difference in either of the two temporal properties when corrected for 3 comparisons using FDR, however, the DMLN CAP showed a trend towards reduced median duration in the HET group in comparison with WT ($p = 0.017$, 2-sample T-test, uncorrected). Differences in the magnitudes of activation and deactivation were found in several voxels for each of the three CAPs as evidenced from the 2-sample T-test maps (bottom panels, Figs. 3A, D, G). These differences are quantified and detailed in the next section.

At the 10-months time point, the LCN and the DMLN CAPs showed significant reduction in their median duration in the HET group ($p = 0.032$, $t(35) = 2.96$ (for LCN CAP), and $p = 0.03$, $t(35) = 2.99$ (for DMLN CAP), 2-sample T-test, FDR corrected for 6 comparisons; Figs. 4B, E) but no difference in their occurrence (Figs. 4C, F). No other CAP showed any significant inter-genotype difference in the duration and the occurrence percentage (Figs. 4H, I, K, L, N, O, Q, R). Two-sample T-test comparisons of spatial patterns between groups showed several prominent differences in the LCN and the DMLN CAPs (bottom panels, Figs. 4A, D). Figures 4G, J, M, P show the other four CAPs and the difference in the voxel-wise activations between WT and HET (bottom panels). As in Figs. 2 and 3, the prominent ROIs considered in the study are shown in Fig. 4S.

Although the optimal number of CAPs was different at each age, there was a high degree of similarity in the spatial patterns of activation and deactivation across ages, especially for the LCN and the DMLN CAPs (Supplementary Fig. 2). The lowest correlation for the LCN CAP was 0.93 between the 3 months and the other two time points. The lowest correlation for the DMLN CAP was 0.68 between the 6 and the 10-months time points. The LCN-DMLN CAP anti-correlation was also observed at all time points with the lowest value of -0.68 observed between the 6-months DMLN and the 10-months LCN CAPs.

Quantification of inter-genotype spatial differences between CAPs.

Next, we quantified the extent of inter-genotype difference in the magnitudes of co-activation and co-deactivation in terms of percentages of all voxels from 28 ROIs. We divided the voxels in each region in three categories for each CAP: (i) co-activated voxels in WT, (ii) co-deactivated voxels in WT and (iii) non-activated voxels in either group. We further subdivided categories (i) and (ii) into 3 sub-categories that showed significant increase, decrease, and non-significant difference in the activation and deactivation magnitude, respectively, in the WT group compared with the HET group.

Figure 5 shows this quantification for the LCN and the DMLN CAP at the three time points while supplementary Fig. 3 shows it for the other CAPs. At all three time points, DMLN regions (cingulate and retrosplenial cortices, in particular) are fully co-activated during the DMLN CAP and co-deactivated during the LCN CAP. The LCN regions (somatosensory and motor cortices, in particular), on the other hand, include both co-activated as well as co-deactivated voxels during both CAPs. In the 3 months LCN CAP, majority of activated voxels showed

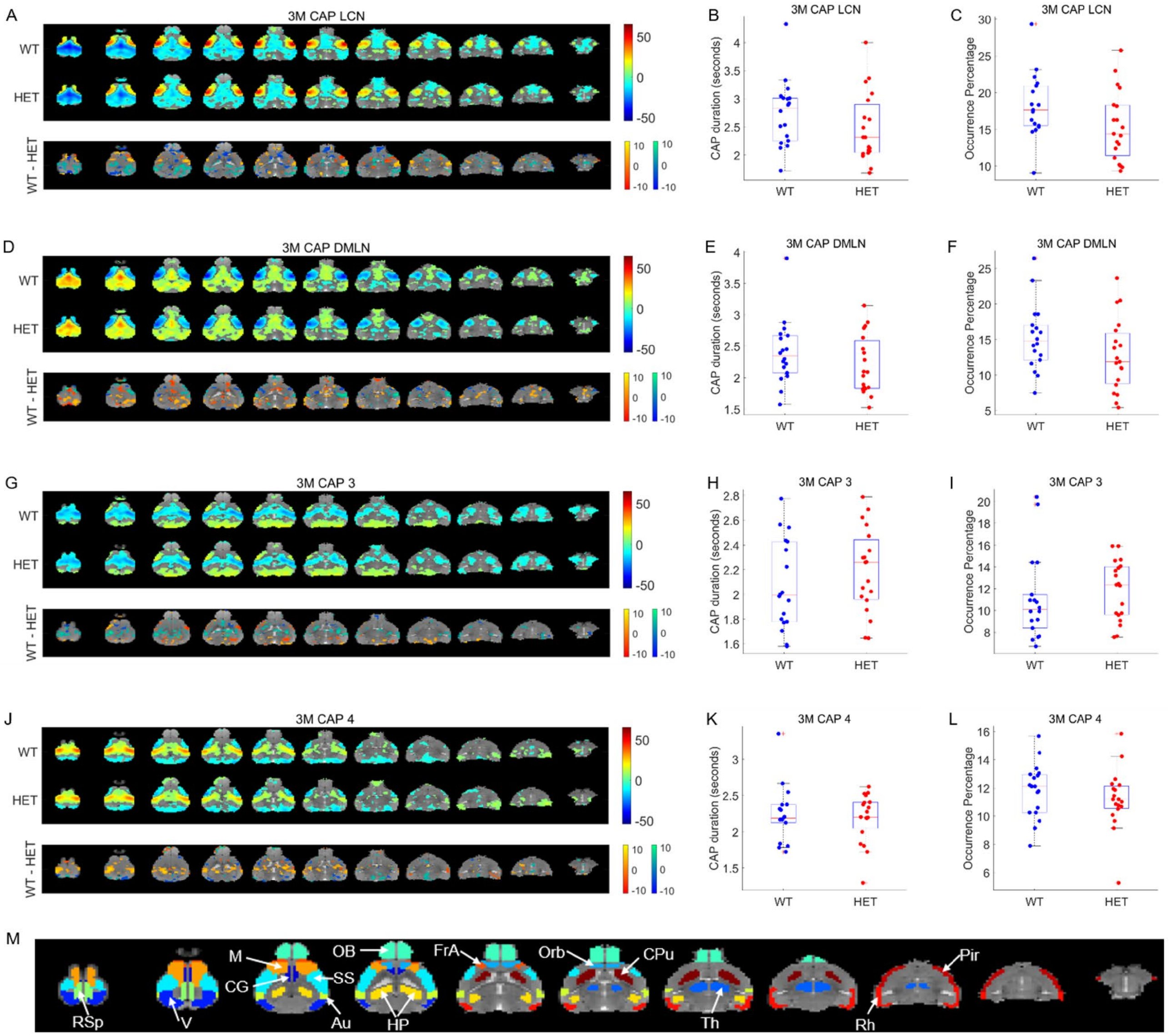

Figure 2. Comparison of spatial and temporal properties of 4 out of 8 CAPs at the 3 months time point. (**A**), (**D**), (**G**), (**J**) top panels show the one-sample T-statistic maps of significantly (Bonferroni corrected, $p < 0.01$) activated and deactivated voxels for each CAP obtained from its occurrences in the WT and HET portions of the combined image-series. Bottom panels show the 2-sample T-test statistic map of voxels with significant (FDR corrected, $p < 0.05$) difference in the (de)activation between the WT and HET CAPs. We make these comparisons for all voxels that are significantly activated or deactivated in either the WT or the HET group. Red-yellow and blue-green colour bars refer to voxels that are co-activated and co-deactivated respectively in the WT group. Thus, positive (yellow, green) and negative (red, blue) T-statistic values respectively indicate significantly lower and higher magnitude of activation in the HET group compared to the WT group. (**B**), (**E**), (**H**), and (**K**) Boxplots of comparisons of median, across subjects, duration of each CAP between WT and HET groups. (**C**), (**F**), (**I**), (**L**) Boxplots of comparison of median occurrence percentage, across subjects, of each CAP between WT and HET groups. (**M**) Fourteen prominent ROIs considered in this study: Retrosplenial cortex (RSp), Visual cortex (V), Motor cortex (M), Cingulate cortex (CG), Olfactory bulb (OB), Somatosensory cortex (SS), Auditory cortex (V), Hippocampus (H), Frontal Association cortex (FrA), Orbital cortex (Orb), Caudate Putamen (CPu), Thalamus (Th), Rhinal cortex (Rh), and Piriform cortex (Pir).

lower deactivation in the right visual and auditory cortices while increased eactivation in the right orbital cortex in the HET group. Prominent changes in the DMLN CAP include lower and higher activation magnitudes in HET in the retrosplenial and cingulate cortices respectively in both hemispheres (Fig. 5A, B). At the 6-months time point, all DMLN regions consistently showed reduced magnitudes of activation and deactivation in HET in the DMLN and LCN CAPs respectively (Fig. 5C, D). Most voxels from the LCN regions also showed reduced magnitude of activation and deactivation in both CAPs in the HET group. Similar reductions in activation

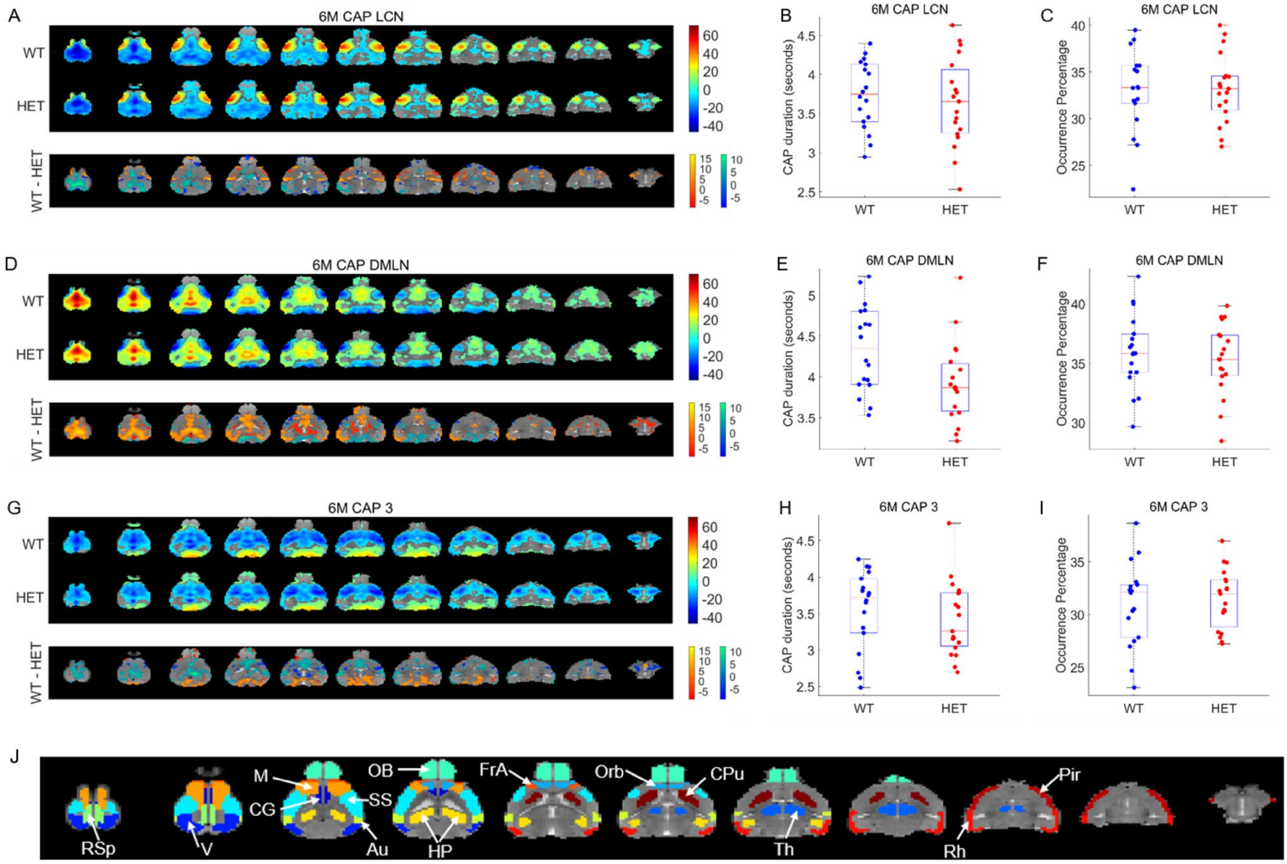

Figure 3. Comparison of spatial and temporal properties of 3 CAPs at the 6-months time point. (**A**), (**D**), (**G**) top panels show the one-sample T-statistic maps of significantly (Bonferroni corrected, $p<0.01$) activated and deactivated voxels for each CAP obtained from its occurrences in the WT and HET portions of the combined image-series. Bottom panels show the 2-sample T-test statistic map of voxels with significant (FDR corrected, $p<0.05$) difference in the (de)activation between the WT and HET CAPs. We make these comparisons for all voxels that are significantly activated or deactivated in either the WT or the HET group. Red-yellow and blue-green colour bars refer to voxels that are co-activated and co-deactivated respectively in the WT group. Thus, positive (yellow, green) and negative (red, blue) T-statistic values respectively indicate significantly lower and higher magnitude of activation in the HET group compared to the WT group. (**B**), (**E**), (**H**) Boxplots of comparisons of median duration, across subjects, of each CAP between WT and HET groups. (**C**), (**F**), (**I**) Boxplots of comparison of median occurrence percentage, across subjects, of each CAP between WT and HET groups. (**J**) Fourteen prominent ROIs considered in this study: Retrosplenial cortex (RSp), Visual cortex (V), Motor cortex (M), Cingulate cortex (CG), Olfactory bulb (OB), Somatosensory cortex (SS), Auditory cortex (V), Hippocampus (H), Frontal Association cortex (FrA), Orbital cortex (Orb), Caudate Putamen (CPu), Thalamus (Th), Rhinal cortex (Rh), and Piriform cortex (Pir).

magnitudes were also found in a majority of voxels from the LCN and the DMLN regions in both CAPs in the HET group at the 10-months time point (Fig. 5E, F).

Classification of WT and HET animals using CAPs. Finally, we assessed the predictive power of CAPs in distinguishing the HET animals from the WT. Temporal properties of CAPs did not perform the classification better than chance at any of the three time points. Spatial properties, however, performed it with significantly higher accuracy than chance at all the three time points (Fig. 6). Here at each age, we used the spatial features for the optimal number of CAPs we found earlier with the entire dataset (Fig. 1). The classification accuracy was significantly higher than chance-level at all three ages and increased with age ($p=1.57\text{E}{-}13$, F (2, 145) = 36.26, one-way ANOVA). Subsequent post-hoc comparisons showed significantly higher mean accuracy of ~ 83% at 10-months than at 3 (~ 60%) and 6 (~ 76%) months time points respectively ($p=1.58\text{E}{-}16$, and 0.026, respectively, Tukey–Kramer corrected for 3 comparisons). Classification accuracy at 6-months was also significantly higher than at 3 months ($p=2.97\text{E}{-}8$, Tukey–Kramer corrected for 3 comparisons). These accuracy levels reflect the robustness of differences in magnitudes of voxel-level activation between the two genotypes, especially at 6 and 10-months of age, when the motor disturbances are reported to be manifested in this model[25].

We also performed the WT versus HET classification using functional connectivity values between 26 regions from both hemispheres (Supplementary Fig. 4)[29]. While FC was significantly more accurate than the chance level at all three ages, the accuracy did not change with age ($p>0.05$, one-way ANOVA). Further, FC-based

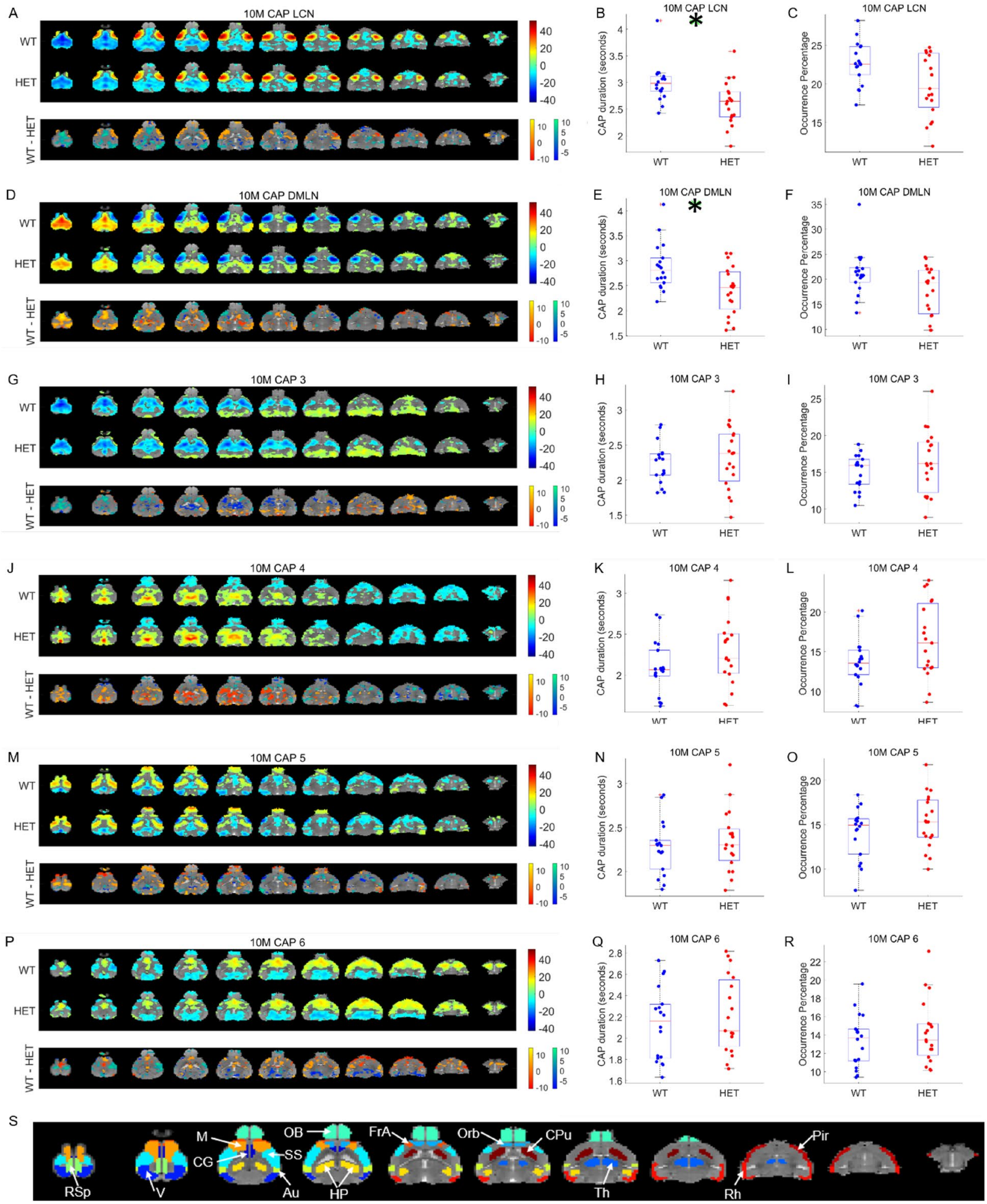

accuracy was significantly lower than CAPs-based at 6-months ($p = 1E{-}3$, $t(98) = 3.39$, two-sample T-test) and at 10-months ($p = 1.6E{-}12$, $t(98) = 8.1$, two-sample T-test).

Discussion

In this longitudinal study, we investigated changes in the transient brain states constituting the resting-state of the brain in a mouse model of HD. We used the zQ175 knock-in DN HET model that shows molecular, cellular, and circuitry alterations that resemble those observed in PwHD[25–27]. Motor disturbances have been reported in this mouse model at 6- and 10-months of age[25].We used the methodology of co-activation patterns in this study. We found that the duration of two prominent, spatially anti-correlated CAPs was reduced in the HET group at 10-months of age. The first CAP, referred to as the lateral-cortical network (LCN) CAP, was characterized by

◂**Figure 4.** Comparison of spatial and temporal properties of 6 CAPs at the 10-months time point. (**A**), (**D**), (**G**), (**J**), (**M**), (**P**) top panels show the one-sample T-statistic maps of significantly (Bonferroni corrected, $p < 0.01$) activated and deactivated voxels for each CAP obtained from its occurrences in the WT and HET portions of the combined image-series. Bottom panel shows the 2-sample T-test statistic map of voxels with significant (FDR corrected, $p < 0.05$) difference in the (de)activation between the WT and HET CAPs. We make these comparisons for all voxels that are significantly activated or deactivated in either the WT or the HET group. Red-yellow and blue-green colour bars refer to voxels that are co-activated and co-deactivated respectively in the WT group. Thus, positive (yellow, green) and negative (red, blue) T-statistic values respectively indicate significantly lower and higher magnitude of activation in the HET group compared to the WT group. (**B**), (**E**), (**H**), (**K**), (**N**), (**Q**) Boxplots of comparisons of median duration, across subjects, of each CAP between WT and HET groups. (**C**), (**F**), (**I**), (**L**), (**O**), (**R**) Boxplots of comparison of median occurrence percentage, across subjects, of each CAP between WT and HET groups. Green asterix indicates significant inter-group difference ($p < 0.05$, Wilcoxon rank-sum test, FDR corrected for 6 comparisons). (**S**) Fourteen prominent ROIs considered in this study: Retrosplenial cortex (RSp), Visual cortex (V), Motor cortex (M), Cingulate cortex (CG), Olfactory bulb (OB), Somatosensory cortex (SS), Auditory cortex (V), Hippocampus (H), Frontal Association cortex (FrA), Orbital cortex (Orb), Caudate Putamen (CPu), Thalamus (Th), Rhinal cortex (Rh), and Piriform cortex (Pir).

simultaneous co-activation and co-deactivation of brain regions constituting the LCN and the default mode like network (DMLN), respectively. The second CAP, called the DMLN CAP, was characterized by the opposite activation topology. At 6-months of age, when most of the phenotypic conversion in motor performance occurs in this model, the DMLN CAP showed a trend for reduction in average duration but the difference was not significant upon correcting for multiple comparisons. None of the CAPs at the early time point of 3 months showed any significant difference in their temporal properties. In terms of spatial properties, magnitude of activation and deactivation was reduced in a large proportion of voxels of the prominent regions belonging to the LCN (somatosensory and motor cortices) and DMLN (anterior cingulate, retrosplenial, visual cortices) CAPs in the HET group at 6 and 10-months of age. At the 3 months time point, a sizeable proportion of voxels in the orbital and the cingulate cortices showed higher activation/deactivation magnitude in the HET group in both LCN as well as DMLN CAPs. Since we could find statistically significant differences especially in the spatial properties of CAPs at all three ages, we investigated their predictive power to distinguish HET animals from the WT. Here, we found that the spatial component of CAPs was. on average, 60% accurate in correctly predicting the genotypic identity of individual test-set subjects at the earliest time point of 3 months. At 6-, and 10-months time points, the accuracy increased to close to 80% reflecting more widespread, robust, and regional level changes occurring as a result of phenotypic progression. We did not find this progressive increase in accuracy with functional connectivity, demonstrating that CAPs, as a representative of dynamic analyses, are more sensitive than static approaches like FC.

We obtained CAPs using a recently improved method[28] that allows clustering of all frames instead of previous approaches where a fraction (typically 15%) of all frames corresponding to supra-threshold BOLD signal of a seed region were clustered[20,30]. This improved method allows a better estimate of temporal properties of CAPs since all frames are partitioned. Here, we concatenated the images of individual mice from both the WT and the HET group in a single image-series before partitioning it to identify the combined CAPs. The advantage of this approach over the separate group-level analysis lies in a joint search for common CAPs in all animals, enabling a direct comparison between groups without a need to match CAPs between groups. In our study, we regressed out the global signal before carrying out the CAP analysis. A previous CAP study in humans has reported results both with and without global signal regression (GSR) and they showed that GSR had little effect on the DMN CAPs involving simultaneous co-activation of DMN regions and co-deactivation of task-positive network (similar to LCN in mice) regions[31]. Since the major differences we found in this study involved an anti-correlated pair of DMLN and LCN CAPs, GSR, per se, is unlikely to be a confound.

At least four CAPs identified at the 3-, and 10-months time points and all three CAPs at the 6-months time point were similar to those previously identified[28]. They also reported that the CAPs occurred in pairs of anti-correlated spatial patterns, a finding we replicated here. The first pair demonstrated simultaneous co-activation of LCN regions such as somatosensory and motor cortices and co-deactivation of DMLN regions that included primarily anterior cingulate, retrosplenial, visual and orbital cortices, and vice versa. Another pair demonstrated widespread cortico-striatal activations and deactivations (only the deactivated pattern was isolated as a CAP at the 6-months time point as the image-series was partitioned into 3 clusters). Spatial patterns of especially the LCN and DMLN CAPs were highly similar across ages.

Duration of the DMLN CAP showed a trend towards a decrease in the HET group at 6-months of age. Both the LCN and DMLN CAPs showed significantly reduced duration in the HET group at 10-months of age. Spatially, we compared the activation strengths of different regions within each CAP between the two groups. In 3 months LCN/DMLN CAPs, we found hyper activation/deactivation in a large percentage of voxels in the cingulate and the retrosplenial cortices that are prominent regions in the DMLN. At 6 and 10-months, when motor disturbances are found in this model, however, we found a significant reduction in the magnitude of activation or deactivation in the majority of voxels in prominent regions belonging especially to the DMLN and the LCN, in the HET group. A recent article shows that the activations in DMLN CAP in mice is correlated with a prominent unimodal-transmodal cortical structural connectivity gradient[32]. Therefore, while we cannot rule out vasculature changes in these regions as an underlying factor for the reductions in the magnitude of activation of both the DMLN and LCN CAPs, they could also be explained by potential changes in the underlying structural connectivity gradients in this mouse model.

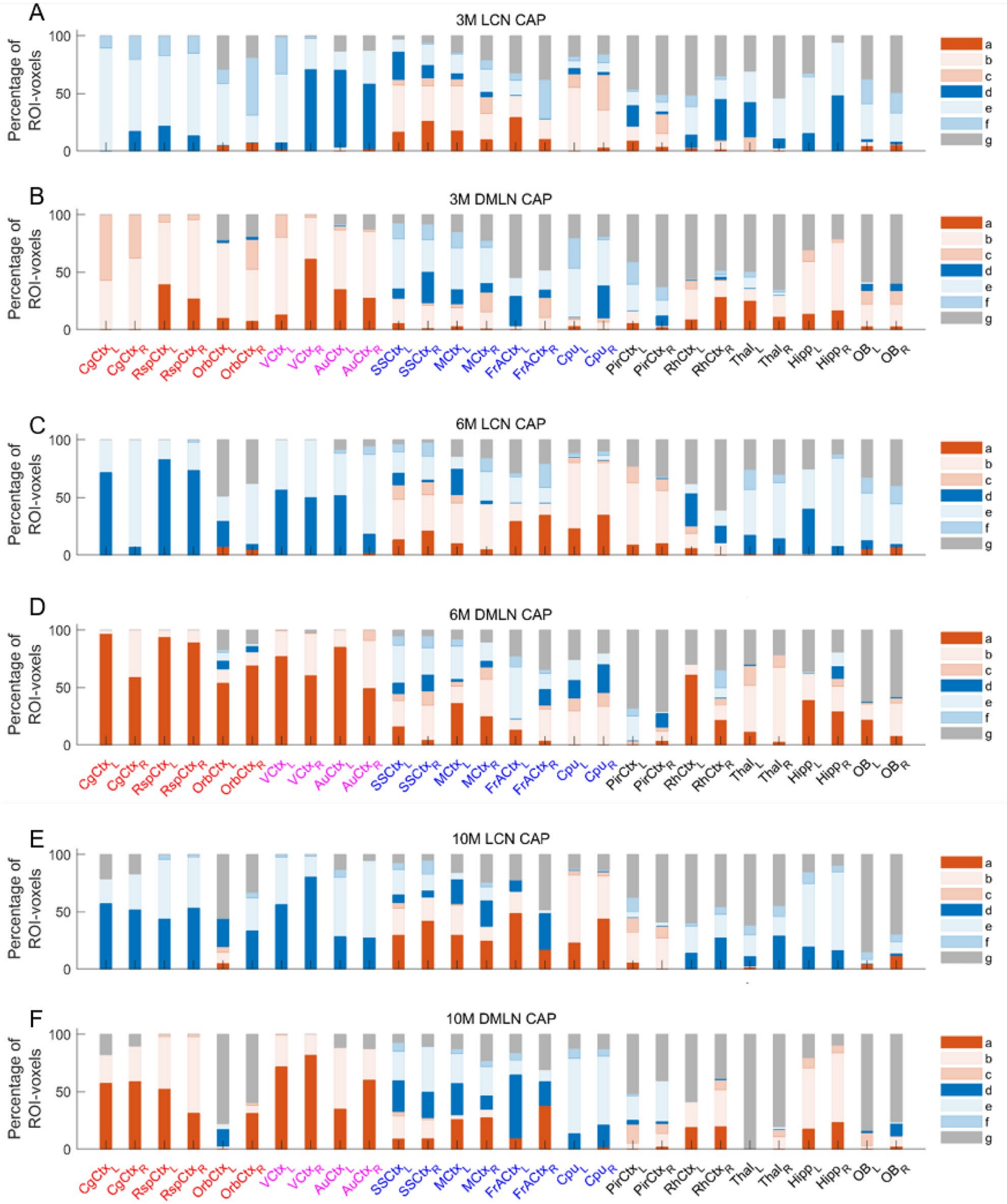

Figure 5. Percentages of voxels per ROI belonging to one of 7 categories for the LCN CAP (A (3 M), C(6 M), E(10 M)) and the DMLN CAP (B (3 M), D(6 M), F(10 M)) respectively. The red & blue colour bars indicate significant co-activation and co-deactivation, respectively, in either the WT or the HET group. Different colour/shade bars indicate percentage of voxels from seven different categories: (**a**) significant co-activation and higher activation magnitude in WT, (**b**) significant co-activation and no significant inter-genotype difference in the activation magnitude, (**c**) significant co-activation and higher activation magnitude in HET, (**d**) significant co-deactivation and higher activation magnitude in WT, (**e**) significant co-deactivation and no significant inter-genotype difference in the activation magnitude, (**f**) significant co-deactivation and higher activation magnitude in HET, and (**g**) non-significant co-activation or co-deactivation during a CAP. Voxel-wise one-sample T-test ($p < 0.01$, Bonferroni corrected) and two-sample T-test ($p < 0.05$, FDR corrected) are performed across occurrences of a CAP within the concatenated genotypic image-series from all subjects to identify the voxels belonging to one of the 7 categories mentioned above in the entire brain. We then calculate the percentages of each category in each of the 28 ROIs shown in Figs. 2M, 3J, 4S. ROIs belonging to the DMLN have red labels, ROIs belonging to the associated cortical network have magenta labels while the blue labels represent LCN ROIs. The black labels represent the rest of the cortical and sub-cortical ROIs.

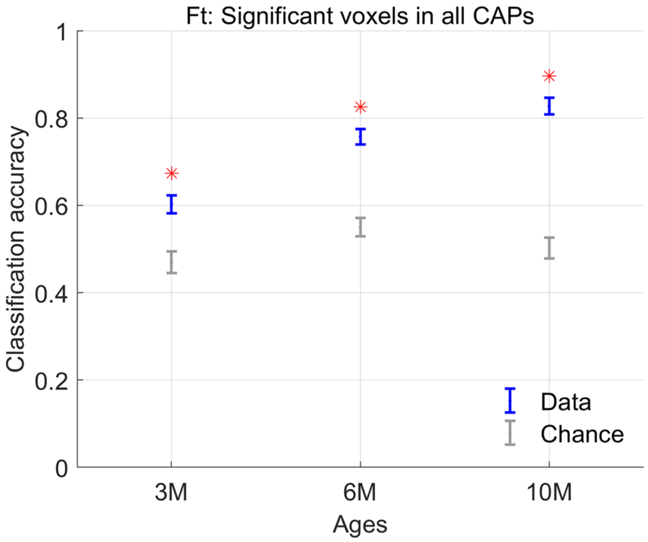

Figure 6. Classification accuracy (blue, mean +/− SEM) using z-scored BOLD signals of voxels with significant activations in 8 CAPs at the 3 months, 3 CAPs at the 6-months, and 6 CAPs at the 10-months time points. The grey error bars show the corresponding chance-level accuracy (mean + / − SEM) and red asterisk indicates significantly higher mean accuracy than the chance level, after correcting for all 3 comparisons ($p < 0.05$; FDR corrected).

Resting-state fMRI based measures are emerging as robust markers of several neurological and neurodegenerative diseases[7–9,33]. One of the prime reasons for this is the non-invasive nature of the scanning protocol. More importantly, task positive networks (TPNs) that are active in specific behavioral tasks such as the motor, attention, and language networks are also active during the resting-state[34]. Hence, alterations within and inter-RSN functional connectivity can be used and has been useful in predicting behavioral deficits in humans[7,35,36]. Changes in the static FC of DMN have been observed in AD patients[37] and found to correlate with levels of amyloid-beta plaque deposits in regions of DMN[38–40]. RSNs such as the default mode and task-positive networks have rodent analogs[41], which means preclinical resting-state fMRI studies in rodent models of disease have high translational value. Going beyond the static FC, Belloy et al. investigated its temporal fluctuations in a transgenic mouse model of AD. They found that short (3 s), spatio-temporal patterns of recurring neural activity, called the quasi-periodic patterns (QPPs), were altered in transgenic mice and that they contributed to the observed static FC changes[42]. In the same cohort we showed that RS-CAPs can predict the identity of transgenic animals accurately[43].

Development of monitoring and response biomarkers is a pressing need in HD research. Most clinical investigations on the impact of HD on the resting-state have focused on the static functional architecture[14]. Preclinical RS-fMRI studies in mouse models of HD[44], including our recently published study[29], have also investigated changes only in static FC. To our knowledge, our study is the first investigation of changes in the transient brain states that make up the resting brain in a mouse model of HD. We find that physiologically prominent brain-states constituting two most robustly observed RSNs – the default-mode like network and the lateral cortical network, and forming the major functional connectivity gradients show the most significant alterations in this mouse model and the changes can be observed from before the observation of motor deficits in this model. The spatiotemporal changes in RS-CAPs at all three ages evaluated in this study prompted us to investigate their predictive power in identifying the status of the HD mouse model. Here, we found nearly 80% accuracy in distinguishing the WT animals from the heterozygous animals when spatial features of CAPs were used at the 6- and 10-months time points. The accuracy was expectedly lower at the 3 months time point, although the classifier performance was significantly better than the chance level. CAPs also performed better than FC in classifying the two genotypic groups at later time points.

Our findings therefore suggest that we can consider RS-CAPs as sensitive markers in this HD mouse model even before phenotypic expression in terms of motor deficits is observed. This is crucial since studies involving animal models of the disease identify early markers, seldom possible in humans. RSNs include spatially distributed brain regions that show high functional connectivity obtained from the entire scan and analogous RSNs have been found in different species. RS-CAPs measure dynamic co-activations and co-deactivations of regions occurring during the scan, thus at shorter time scales than the RSNs. However, similar to RSNs, RS-CAPs – especially a pair of anti-correlated CAPs involving simultaneous co-activations and co-deactivations of default-mode like and lateral-cortical networks – have been identified across species including humans[21]. Therefore, investigation of changes in properties of CAPs in a disease context has potential translational value. Further, as there is a high degree of similarity in functional networks active during behavioral tasks and the resting-state, we can speculate that changes in RS-CAPs may be predictive of functional changes at the behavioral level. Therefore, findings from our study make a strong case to investigate RS-CAPs in a clinical setting in order to find out if they can be, first, predictive of the human disease and, next, predictive of behavioral impairments and/or stages of the disease in patients.

Limitations. Although this was a longitudinal study, we did not test, statistically, the age effect on the spatial and temporal properties of CAPs and their genotypic alterations. We followed this approach mainly driven by the observation that we find different optimal number of CAPs per age. Methodological limitations of dynamic analyses such as CAPs require concatenated data from multiple subjects to extract the transient brain states. Therefore, in order to ensure that the properties of the same CAP are compared longitudinally, we need to concatenate data from all subjects at all three ages before running the clustering algorithm. When we clustered concatenated data from all subjects at all ages, 6 CAPs were found to be optimal. We found diminished inter-genotypic differences at each age in these CAPs, indicating that they have lowered sensitivity to detect HET vs. WT mice differences. In our view, these results confirm the suspicion that forcing all CAPs to represent all age groups at once may result in suboptimal solutions in which individual CAPs capture better the common variance occurring at all ages at the expense of the age-specific activation patterns. It is important to note that there is multiple evidence that the evolution of anomalies in Huntington's disease is not linear (for examples with human fMRI findings, see Pini 2020). With anomalies that evolve non-linearly over time, it may be more productive for the research community to focus on the age-specific (or stage-specific) anomalies rather than pushing for solutions that seek to find common patterns across all ages (or stages). A second limitation was that we used only males in this study. This decision was based on a previous study that found sex-based differences in the zQ175 mouse model, where males recapitulated abnormal volume changes that have been observed in human HD, but female zQ175 mice lack to show those changes[45]. Nevertheless, currently ongoing studies in our group on other mouse models of HD and planned future studies include both males and females.

Materials and methods

Ethical statement. All procedures were performed in strict accordance with the European Directive 2010/63/EU on the protection of animals used for scientific purposes. The protocols were approved by the Committee on Animal Care and Use at the University of Antwerp, Belgium (permit number 2017–09) and all efforts were made to minimize animal suffering. The reporting in the manuscript follows the recommendations in ARRIVE guidelines.

Animals. zQ175 delta neo (DN, neomycin-sensitive cassette excised), knock-in heterozygous mouse model is used in this study. The neo + version of the model used in earlier studies showed a close resemblance in molecular, cellular and circuitry alterations of human Huntington's disease[25,26]. Most of the phenotypic conversion in motor performance in the heterozygous zQ175 DN model[27] happens around 6-months of age. The cohort used in this study consisted of 20 male zQ175 DN heterozygous (referred henceforth as HET) mice and 19 age-matched wild-type (WT) littermates. RS-fMRI data were collected longitudinally at three time points when the animals were 3, 6, and 10-months of age. One animal from each group was found to be mis-genotyped, hence both animals were excluded from the analysis. Thus, the analysis was performed on 18 WT and 19 HET animals.

RS-fMRI data acquisition. The mice were initially anesthetized with 2% isoflurane (IsoFlo, Abbott, Illinois, USA) in a mixture of 200 ml/min nitrogen and 400 ml/min oxygen. Heads were fixed with bite and ear bars. Ophthalmic ointment was applied to the eyes. Animal core body temperature was monitored with a rectal temperature probe and kept stable at 37 °C via hot air supply (MR-compatible Small Animal Heating System, SA Instruments, Inc.). A pressure sensitive pad and a fiber-optic pulse oximeter placed over the tail were used to monitor the breathing rate and the heart rate & O2 saturation (MR-compatible Small Animal Monitoring and Gating system, SA Instruments, Inc.) respectively. Following animal handling, the mice received a bolus injection of medetomidine (0.075 mg/kg; Domitor, Pfizer, Karlsruhe, Germany) after which the isoflurane level was reduced to 0.4% over the course of 30 min. Throughout the entire imaging protocol, the isoflurane level was maintained at this level. A subcutaneous catheter allowed continuous infusion of medetomidine (0.15 mg/kg/hr) starting 10 min after bolus injection, resembling a brain state of rest[46]. The RS-fMRI acquisition started 40 min after bolus injection. After the MRI procedure, the effect of medetomidine was counteracted by injecting 0.1 mg/kg atipamezole (Antisedan, Pfizer, Karlsruhe, Germany).

MRI scans were performed on a 9.4 T Biospec Bruker system (Germany) using a mouse head receiver 2 × 2 array cryo-coil. RS-fMRI data were acquired with a single shot gradient-echo echo-planar imaging (EPI) sequence, field of view (27 × 21) mm[2], matrix dimensions (MD) [90,70], 12 horizontal slices with 0.4 mm thickness, in-plane resolution (300 × 300) µm[2], flip angle 60°, bandwidth 400 kHz, repetition time (TR) 500 ms, echo time (TE) 15 ms, 1200 repetitions. 3D RARE images were acquired, in order to create a study specific 3D template, with TR 1800 ms, TE 42 ms, MD [256,256,128], isotropic resolution (78 × 78 × 78) µm[3].

Pre-processing of functional MRI data. RS-fMRI data of each subject were realigned to the first-time frame using the least-squares approach and a 6-parameter rigid body spatial transformation. A study-based 3D template was generated in Advanced Normalization Tools (ANTs), using individual 3D RARE images from 1/3 of the subjects from each group at each time point. Transformation parameters were extracted from two different normalization steps, where each RS-fMRI scan was registered to the corresponding subject 3D RARE image acquired at the same time point, and each subject 3D RARE scan was normalized to the study-based template. Moreover, spatial normalization parameters were calculated between the study-based template and an in-house C57BL6 mouse brain atlas. Finally, the RS-fMRI data were spatially normalized to the in-house atlas by combining the previous normalization estimation parameters (RS-fMRI to 3D RARE, 3D RARE to study template and study template to in-house atlas). Next, we performed in-plane smoothing using a Gaussian kernel with full width at half maximum of twice the voxel size. Motion vectors were then regressed out of the image-series. These procedures were performed using Statistical Parametric Mapping (SPM12) software (Welcome Department of Cognitive Neurology, London, UK).

Images were then filtered voxel-wise using a 0.01–0.2 Hz Butterworth band-pass filter, and quadratic detrended. Five-time frames at the start and the end of the scan were excluded before and after filtering to avoid transient effects and to minimize boundary effects of filtering respectively. Global signal, obtained using a whole brain mask, was regressed out from the BOLD signal of each voxel that was then normalized to zero mean and unit variance. We used in-house MATLAB scripts for filtering, detrending, global signal regression and z-scoring.

CAP analysis. Since cerebellar BOLD signal was found to be anti-correlated with most regions in the cerebrum, this strong anti-correlation masked the relationships between regions of the cerebrum, which is our main interest here. Hence, specifically, for the CAP analysis, we used a mask excluding the cerebellum. We assessed temporal fluctuations of neural activity in terms of instantaneous BOLD CAPs following an approach by Gutierrez-Barragan et al.[28] using a combined image-series from both WT and HET animals for each time point separately. Specifically, we first concatenated the processed image volumes from each animal from both genotypes to form a combined image-series. Then, we transformed this image-series into N, m-dimensional vectors where N is the total number of frames from all subjects and m is the total number of voxels within the mask mentioned above. We then divided all time frames using a K-means++ algorithm into clusters showing similar spatial activation patterns. We did this by assessing the spatial dissimilarity of the whole-brain activation pattern of each frame with that of every other frame using the correlation distance (1—Pearson's correlation) between every pair of m-dimensional vectors. The algorithm partitions the vector set into K clusters such that the sum of within cluster-distance $D = \sum_{k=1}^{K}\sum_{j\in k}d^2\left(z_j, c_k\right)$ is minimized. Here, K is a predefined number of clusters and $d\left(z_j, c_k\right)$ denotes the correlation distance between the centroid c_k of the kth cluster and jth time frame belonging to the kth cluster. The k-means++ algorithm provides an optimal choice of initial cluster centroids as seeds so that distant centroids have a greater chance of getting selected as initial centroids. We varied the number of time frame clusters from 2 to 20, and in each case calculated the across-subject variance explained by the clustering solution as follows[47]:

- Within cluster variance, $V_w = \frac{1}{N}\sum_{k=1}^{K}\sum_{j\in k}d^2\left(z_j, c_k\right)$ where, N is the total number of observations (time frames); K is number of clusters and $d\left(z_j, c_k\right)$ denotes the correlation distance between the centroid c_k of the k^{th} cluster and j^{th} observation belonging to the k^{th} cluster.
- Between cluster variance, $V_B = \frac{1}{N}\sum_{k=1}^{K}n_k d^2(c_k, \boldsymbol{c})$; $\boldsymbol{c} = \sum_{k=1}^{K}\frac{n_k}{N}c_k$ where $d(c_k, \boldsymbol{c})$ is the correlation distance between the global centroid $\boldsymbol{c}$ and the k^{th} cluster's centroid c_k and n_k is the number of time frames in the k^{th} cluster.
- Explained variance $= \frac{V_B}{V_w + V_B}$

We then plotted the explained variance as a function of partitions of the image-series with increasing number of clusters (in the range from 2 to 20) and identified the minimum number at which the variance reached a saturation level (elbow point) as the optimal number of clusters. We also calculated, for each partition of k clusters, the fractional gain in explained variance over and above the variance explained by the partition of k-1 clusters. We further ensured the variance saturation at the elbow point by verifying that for all partitions with higher numbers of clusters this fractional gain in explained variance remained below 0.005[28]. Voxel-wise averaging of signal intensities was carried out across all time frames within each cluster to produce combined CAPs. Similarly, averaging across the genotype-specific time frames within each cluster was carried out to obtain the WT and the HET group-level CAPs.

We then performed a one-sample two-tailed T-test to test the mean activation, across the occurrences of each CAP in the combined image-series as well as the WT or HET sections of it, of each voxel against a null hypothesis of zero activation and corrected for multiple comparisons using the Bonferroni correction ($p < 0.01$). The voxels that showed significant activation or deactivation constituted the one-sample T-statistic maps for each CAP, representing the regional activities that constitute the CAP. We then calculated the temporal and spatial properties for each of the CAPs for each subject within each genotype group:

1. Occurrence percentage: the percentage of the time frames corresponding to a CAP within a subject's image-series.
2. Duration: number of consecutive frames corresponding to a CAP, averaged across all its occurrences, within a subject.
3. Voxel-level activations: Mean activation across all occurrences of a CAP within a genotype group-level image-series (WT/HET portions of combined image series).

Regions of interest (ROIs). In order to compare the spatial properties of individual CAPs between the two genotypes, we obtained the mean activation in 28 bilateral ROIs in addition to voxel-level activation. These regions were selected based on their size (number of voxels > 30) and their relevance for the CAPs. These 28 anatomical ROIs were:

1. Default-mode like network (DMLN) regions: Cingulate (CgCtx), retrosplenial (RspCtx), and orbital (OrbCtx) cortices.
2. Associated cortical network (ACN) regions: Auditory (AuCtx) and Visual (VCtx) cortices.

3. Lateral cortical network (LCN) regions: Somatosensory (SSCtx), Motor (MCtx), Frontal Association (FrCtx) cortices and the Caudate putamen (CPu).
4. Other cortical and sub-cortical regions: Piriform (PirCtx), Rhinal (RhCtx), Thalamus (Th), Hippocampus (Hp) and the Olfactory bulb (OB).

Statistical comparisons. We first compared, between genotypes at each time point, the median duration and occurrence percentage across subjects, for each of the optimal number of CAPs identified using the explained variance approach mentioned above. Mean activation levels of significantly activated ($p < 0.01$, 1-sample T-test, Bonferroni corrected) voxels in either the WT or the HET group for each of these CAPs across their occurrences were compared between genotypes using a 2-sample T-test and corrected for multiple comparisons using the Benjamini–Hochberg correction[48] for controlling the false discovery rate (FDR). The voxels that showed significant inter-genotype difference in activation constituted the 2-sample T-test statistic map and their T-statistics were displayed using two colormaps depending on whether they were activated or deactivated in the WT.

Classification. In order to classify HET animals from WT at each time point, we used a multinomial logistic regression (MLR) with regularization as a classifier. We trained the classifier using properties of CAPs on 80% of the subjects ($n = 29$) constituting the training set, chosen randomly but in a genotype-stratified manner, and tested its accuracy on the remaining 20% ($n = 8$) constituting the validation set. As all subjects were used to obtain group-level CAPs, information on validation set subjects could bias the classifier to predict them more accurately than otherwise possible. In order to avoid this bias, we modified the CAP extraction procedure to avoid cross-contamination during the classification procedure. For this, we first extracted K (*$K = 8$ at 3 months, 3 at 6-months and 6 at 10-months*) group-level CAPs (gCAP) from only the training set and then obtained the subject-level CAPs for each training and test-set subject as follows. First, we calculated spatial correlation between each of the K gCAPs and the image-series of every subject using only the significantly activated voxels in that gCAP. Then every time frame in subject's image-series was assigned a label between 1 and K reflecting the gCAP with which it had the highest correlation. The frames with the same label were voxel-wise averaged to construct the corresponding CAP for every subject.

After obtaining K subject-level CAPs, we trained the classifier using their spatial and temporal properties in the training set subjects. Specifically, for each of the K CAPs we pooled either, (a) duration and occurrence rate (the temporal component), or (b) BOLD intensities of voxels whose activations within the corresponding gCAP were found to be significantly different from zero (the spatial component). These computed scores from each subject were z-scored within each subject so that their relative rankings, and not the absolute values, were used as input features for classification. The regularization parameter in the MLR classifier was set to 10 to control for over-fitting. This value was estimated using a grid search algorithm for estimation of hyper-parameters. The classifier was tested on the validation set and classification accuracy was obtained. We then shuffled the class identities (WT/HET) across all subjects and using the same training and test-set, obtained a chance level accuracy in each case.

We repeated the accuracy calculation on 50 trials of randomly sampled, genotype stratified train and validation sets and statistically compared the median classification accuracy with median chance-level accuracy. As both the real and chance-level accuracy values for each split were obtained using identical training and test features (but different class identities), we performed this comparison using the Wilcoxon signed-rank test which allows comparison of paired samples. Median chance-level accuracy was expected to be ~ 50% as the number of subjects in each group was nearly equal.

Data availability

The datasets used and/or analysed during the current study are available on the Mendeley data repository (http://dx.doi.org/10.17632/dvtbkxwwhb.1, and https://dx.doi.org/10.17632/5r3nytnw2y.1). They are under embargo until September 2, 2023 and will be made public after that date. During the embargo period, they can be accessed upon request to the corresponding author.

Received: 22 December 2022; Accepted: 10 June 2023

References

1. Bates, G. P. *et al.* Huntington disease. *Nat. Rev. Dis. Primer* **1**, 1–21. https://doi.org/10.1038/nrdp.2015.5 (2015).
2. Paoli, R. A. *et al.* Neuropsychiatric burden in Huntington's disease. *Brain Sci.* **7**, 67. https://doi.org/10.3390/brainsci7060067 (2017).
3. Ross, C. A. & Tabrizi, S. J. Huntington's disease: from molecular pathogenesis to clinical treatment. *Lancet Neurol.* **10**, 83–98. https://doi.org/10.1016/S1474-4422(10)70245-3 (2011).
4. Nanetti, L. *et al.* Cortical thickness, stance control, and arithmetic skill: An exploratory study in premanifest Huntington disease. *Parkinsonism Relat. Disord.* **51**, 17–23. https://doi.org/10.1016/j.parkreldis.2018.02.033 (2018).
5. Rosas, H. D. *et al.* Cerebral cortex and the clinical expression of Huntington's disease: Complexity and heterogeneity. *Brain* **131**, 1057–1068. https://doi.org/10.1093/brain/awn025 (2008).
6. Baldassarre, A. *et al.* Large-scale changes in network interactions as a physiological signature of spatial neglect. *Brain* https://doi.org/10.1093/brain/awu297 (2014).
7. Siegel, J. S. *et al.* Disruptions of network connectivity predict impairment in multiple behavioral domains after stroke. *Proc. Natl. Acad. Sci.* **113**, E4367–E4376. https://doi.org/10.1073/pnas.1521083113 (2016).
8. Di Perri, C. *et al.* Multifaceted brain networks reconfiguration in disorders of consciousness uncovered by co-activation patterns. *Hum. Brain Mapp.* **39**, 89–103. https://doi.org/10.1002/hbm.23826 (2018).

9. Badhwar, A. *et al.* Resting-state network dysfunction in Alzheimer's disease: A systematic review and meta-analysis. *Alzheimers Dement. Diagn. Assess. Dis. Monit.* **8**, 73–85. https://doi.org/10.1016/j.dadm.2017.03.007 (2017).
10. Buckner, R. L. *et al.* Molecular, structural, and functional characterization of Alzheimer's Disease: Evidence for a relationship between default activity, amyloid, and memory. *J. Neurosci.* **25**, 7709–7717. https://doi.org/10.1523/JNEUROSCI.2177-05.2005 (2005).
11. Poudel, G. R. *et al.* Abnormal synchrony of resting state networks in premanifest and symptomatic Huntington disease: the IMAGE-HD study. *J. Psychiatry Neurosci. JPN* **39**, 87–96. https://doi.org/10.1503/jpn.120226 (2014).
12. Werner, C. J. *et al.* Altered resting-state connectivity in Huntington's Disease. *Hum. Brain Mapp.* **35**, 2582–2593. https://doi.org/10.1002/hbm.22351 (2014).
13. Wolf, R. C. *et al.* Abnormal resting-state connectivity of motor and cognitive networks in early manifest Huntington's disease. *Psychol. Med.* **44**, 3341–3356. https://doi.org/10.1017/S0033291714000579 (2014).
14. Pini, L. *et al.* Aberrant brain network connectivity in presymptomatic and manifest Huntington's disease: A systematic review. *Hum. Brain Mapp.* **41**, 256–269. https://doi.org/10.1002/hbm.24790 (2020).
15. Allen, E. A. *et al.* Tracking whole-brain connectivity dynamics in the resting state. *Cereb. Cortex N. Y. N* **1991**(24), 663–676. https://doi.org/10.1093/cercor/bhs352 (2014).
16. Deco, G., Kringelbach, M. L., Jirsa, V. K. & Ritter, P. The dynamics of resting fluctuations in the brain: Metastability and its dynamical cortical core. *Sci. Rep.* **7**, 3095. https://doi.org/10.1038/s41598-017-03073-5 (2017).
17. Hutchison, R. M. *et al.* Dynamic functional connectivity: promise, issues, and interpretations. *Neuroimage* **80**, 360–378. https://doi.org/10.1016/j.neuroimage.2013.05.079 (2013).
18. Hindriks, R. *et al.* Can sliding-window correlations reveal dynamic functional connectivity in resting-state fMRI?. *Neuroimage* **127**, 242–256. https://doi.org/10.1016/j.neuroimage.2015.11.055 (2016).
19. Zalesky, A., Fornito, A., Cocchi, L., Gollo, L. L. & Breakspear, M. Time-resolved resting-state brain networks. *Proc. Natl. Acad. Sci.* **111**, 10341–10346. https://doi.org/10.1073/pnas.1400181111 (2014).
20. Liu, X. & Duyn, J. H. Time-varying functional network information extracted from brief instances of spontaneous brain activity. *Proc. Natl. Acad. Sci.* **110**, 4392–4397. https://doi.org/10.1073/pnas.1216856110 (2013).
21. Liu, X., Zhang, N., Chang, C. & Duyn, J. H. Co-activation patterns in resting-state fMRI signals. *Neuroimage* **180**, 485–494. https://doi.org/10.1016/j.neuroimage.2018.01.041 (2018).
22. Majeed, W. *et al.* Spatiotemporal dynamics of low frequency BOLD fluctuations in rats and humans. *Neuroimage* **54**, 1140–1150. https://doi.org/10.1016/j.neuroimage.2010.08.030 (2011).
23. Thompson, G. J., Pan, W.-J., Magnuson, M. E., Jaeger, D. & Keilholz, S. D. Quasi-periodic patterns (QPP): Large-scale dynamics in resting state fMRI that correlate with local infraslow electrical activity. *Neuroimage* https://doi.org/10.1016/j.neuroimage.2013.09.029 (2014).
24. Belloy, M. E. *et al.* Dynamic resting state fMRI analysis in mice reveals a set of quasi-periodic patterns and illustrates their relationship with the global signal. *Neuroimage* **180**, 463–484. https://doi.org/10.1016/j.neuroimage.2018.01.075 (2018).
25. Heikkinen, T. *et al.* Rapid and robust patterns of spontaneous locomotor deficits in mouse models of Huntington's disease. *PLoS ONE* **15**, e0243052. https://doi.org/10.1371/journal.pone.0243052 (2020).
26. Menalled, L. B. *et al.* Comprehensive behavioral and molecular characterization of a new knock-in mouse model of Huntington's disease: zQ175. *PLoS ONE* **7**, e49838. https://doi.org/10.1371/journal.pone.0049838 (2012).
27. Southwell, A. L. *et al.* An enhanced Q175 knock-in mouse model of Huntington disease with higher mutant huntingtin levels and accelerated disease phenotypes. *Hum. Mol. Genet.* **25**, 3654–3675. https://doi.org/10.1093/hmg/ddw212 (2016).
28. Gutierrez-Barragan, D., Basson, M. A., Panzeri, S. & Gozzi, A. Infraslow state fluctuations govern spontaneous fMRI network dynamics. *Curr. Biol.* **29**, 2295-2306.e5. https://doi.org/10.1016/j.cub.2019.06.017 (2019).
29. Vasilkovska, T. *et al.* Resting-state fMRI reveals longitudinal alterations in brain network connectivity in the zQ175DN mouse model of Huntington's disease. *Neurobiol. Dis.* **181**, 106095. https://doi.org/10.1016/j.nbd.2023.106095 (2023).
30. Karahanoğlu, F. I. & Ville, D. V. D. Transient brain activity disentangles fMRI resting-state dynamics in terms of spatially and temporally overlapping networks. *Nat. Commun.* **6**, 7751. https://doi.org/10.1038/ncomms8751 (2015).
31. Liu, X., & Duyn, J. H. Resting-state fMRI signal anti-correlation exists in absence of global signal regression. In *Proceedings of the 21st ISMRM Annual Meeting* (2013)
32. Coletta, L. *et al.* Network structure of the mouse brain connectome with voxel resolution. *Sci. Adv.* **6**, eabb7187. https://doi.org/10.1126/sciadv.abb7187 (2020).
33. Adhikari, M. H. *et al.* Decreased integration and information capacity in stroke measured by whole brain models of resting state activity. *Brain J. Neurol.* **140**, 1068–1085. https://doi.org/10.1093/brain/awx021 (2017).
34. Vincent, J. L. *et al.* Intrinsic functional architecture in the anaesthetized monkey brain. *Nature* **447**, 83–86. https://doi.org/10.1038/nature05758 (2007).
35. Ramsey, L. E. *et al.* Normalization of network connectivity in hemispatial neglect recovery. *Ann. Neurol.* **80**, 127–141. https://doi.org/10.1002/ana.24690 (2016).
36. Tavor, I. *et al.* Task-free MRI predicts individual differences in brain activity during task performance. *Science* **352**, 216–220. https://doi.org/10.1126/science.aad8127 (2016).
37. Mevel, K., Chételat, G., Eustache, F. & Desgranges, B. The default mode network in healthy aging and Alzheimer's disease. *Int. J. Alzheimer's Dis.* https://doi.org/10.4061/2011/535816 (2011).
38. Koch, K. *et al.* Disrupted intrinsic networks link amyloid-β pathology and impaired cognition in prodromal Alzheimer's disease. *Cereb. Cortex* **25**, 4678–4688. https://doi.org/10.1093/cercor/bhu151 (2015).
39. Myers, N. *et al.* Within-patient correspondence of amyloid-β and intrinsic network connectivity in Alzheimer's disease. *Brain* **137**, 2052–2064. https://doi.org/10.1093/brain/awu103 (2014).
40. Sperling, R. A. *et al.* Amyloid deposition is associated with impaired default network function in older persons without dementia. *Neuron* **63**, 178–188. https://doi.org/10.1016/j.neuron.2009.07.003 (2009).
41. Gozzi, A. & Schwarz, A. J. Large-scale functional connectivity networks in the rodent brain. *Neuroimage* **127**, 496–509. https://doi.org/10.1016/j.neuroimage.2015.12.017 (2016).
42. Belloy, M. E. *et al.* Quasi-periodic patterns of neural activity improve classification of Alzheimer's disease in mice. *Sci. Rep.* **8**, 10024. https://doi.org/10.1038/s41598-018-28237-9 (2018).
43. Adhikari, M. H., Belloy, M. E., Van der Linden, A., Keliris, G. A. & Verhoye, M. Resting-state co-activation patterns as promising candidates for prediction of Alzheimer's disease in aged mice. *Front. Neural Circuits* https://doi.org/10.3389/fncir.2020.612529 (2021).
44. Li, Q. *et al.* Resting-state functional MRI reveals altered brain connectivity and its correlation with motor dysfunction in a mouse model of Huntington's disease. *Sci. Rep.* **7**, 16742. https://doi.org/10.1038/s41598-017-17026-5 (2017).
45. Zhang, C. *et al.* Abnormal brain development in huntington' disease is recapitulated in the zQ175 knock-in mouse model. *Cereb. Cortex Commun.* **1**, tgaa044. https://doi.org/10.1093/texcom/tgaa044 (2020).
46. Jonckers, E. *et al.* Different anesthesia regimes modulate the functional connectivity outcome in mice. *Magn. Reson. Med.* **72**, 1103–1112. https://doi.org/10.1002/mrm.24990 (2014).
47. Goutte, C., Toft, P., Rostrup, E., Nielsen, F. Å. & Hansen, L. K. On clustering fMRI time series. *Neuroimage* **9**, 298–310. https://doi.org/10.1006/nimg.1998.0391 (1999).

48. Benjamini, Y. & Hochberg, Y. Controlling the false discovery rate: A practical and powerful approach to multiple testing. *J. R. Stat. Soc. Ser. B Methodol.* **57**, 289–300 (1995).

Author contributions

M.H.A. designed the study and the analysis, carried out the analysis, prepared all figures, and wrote the main manuscript. T.V. contributed to the study design, acquired and pre-processed the data, and gave inputs on the manuscript. R.C., H.T., L.L., G.A.K., I.M.S., D.P., and A.V.L. contributed inputs to the study design and/or the methodology and reviewed the manuscript. M.V. designed the study, contributed inputs to the methodology, supervised the study, and wrote the manuscript.

Funding

This work was funded by CHDI Foundation, Inc., a nonprofit biomedical research organization exclusively dedicated to developing therapeutics that will substantially improve the lives of HD-affected individuals. The computational resources and services used in this work were provided by the HPC core facility CalcUA of the University of Antwerp, the VSC (Flemish Supercomputer Center), funded by the Hercules Foundation, and the Flemish Government department EWI. The work was also supported by the Flemish Impulse funding for heavy scientific equipment under Grant Agreement No. OZ3544 (Granted to Annemie Van der Linden).

Competing interests

The authors declare no competing interests.

Additional information

Supplementary Information The online version contains supplementary material available at https://doi.org/10.1038/s41598-023-36812-y.

Correspondence and requests for materials should be addressed to M.H.A.

Reprints and permissions information is available at www.nature.com/reprints.